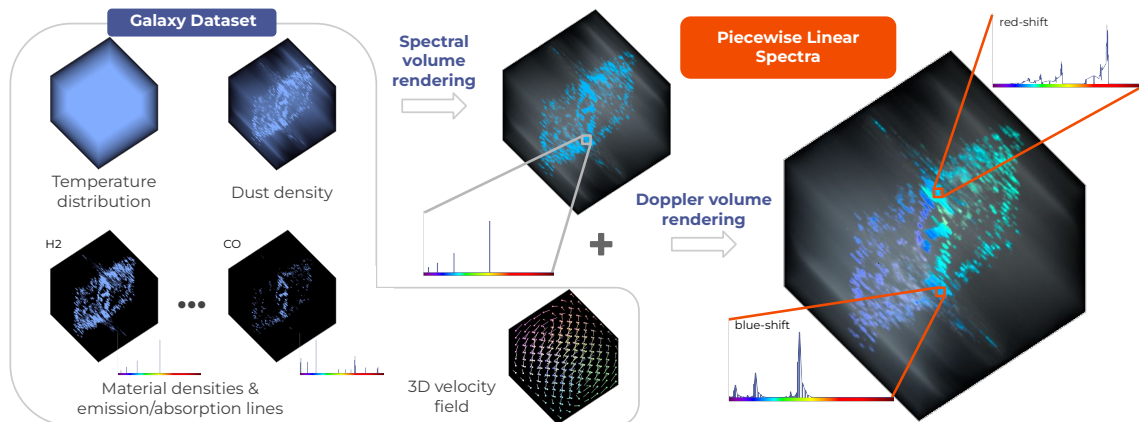


# Doppler Volume Rendering: A Dynamic, Piecewise Linear Spectral Representation for Visualizing Astrophysics Simulations

Reem Alghamdi<sup>1</sup>, Thomas Müller<sup>2</sup>, Alberto Jaspe-Villanueva<sup>1</sup>, Markus Hadwiger<sup>1</sup>, Filip Sadlo<sup>3</sup>

<sup>1</sup>KAUST, Saudi Arabia, <sup>2</sup>Max-Planck-Institute for Astronomy, Germany, <sup>3</sup>Heidelberg University, Germany



**Figure 1:** Doppler volume rendering applied to the Galaxy dataset, consisting of different volumetric species, such as hydrogen ( $H_2$ ) and carbon monoxide ( $CO$ ), accompanied by a 3D velocity field describing their motion. Spectral volume rendering based on our novel piecewise linear spectral representation enables inclusion of the involved Doppler effect, and at the same time high accuracy at interactive frame rates.

## Abstract

We present a novel approach for rendering volumetric data including the Doppler effect of light. Similar to the acoustic Doppler effect, which is caused by relative motion between a sound emitter and an observer, light waves also experience compression or expansion when emitter and observer exhibit relative motion. We account for this by employing spectral volume rendering in an emission-absorption model, with the volumetric matter moving according to an accompanying vector field, and emitting and attenuating light at wavelengths subject to the Doppler effect. By introducing a novel piecewise linear representation of the involved light spectra, we achieve accurate volume rendering at interactive frame rates. We compare our technique to rendering with traditional point-based spectral representation, and demonstrate its utility using a simulation of galaxy formation.

## CCS Concepts

- Human-centered computing → Scientific visualization; • Computing methodologies → Simulation evaluation;

## 1. Introduction

3D scalar fields are widely present in science and engineering, either measured, as in the case of computed tomography in medicine, or simulated, as in the case of galaxy formation in astrophysics. Volume rendering provides an effective means to visualize such fields, by assigning emission and absorption properties to the scalar field using so-called transfer functions, and by accumulating these effects along view rays using ray casting. Emission, absorption,

and accumulation are typically carried out in RGB color space, but the approach has been extended to spectral representation, enabling more realistic physical optical effects. Such spectral accumulation is traditionally carried out in point-based spectral representation, resulting, however, in computation times far beyond interactivity, in particular for sufficiently accurate results. On the other hand, spectral volume rendering has many advantages, such as a physically correct representation of light flux, and realistic modeling of translucent materials, e.g., wavelength-dependent transparency.

Moreover, spectral volume rendering can deal with electromagnetic emission outside the visible range, such as infrared or ultraviolet.

When dealing with data of extreme physical magnitudes, such as astrophysical simulations, additional important aspects of the physics of light need to be considered. One of the most important effects is the Doppler effect, which is commonly known for sound waves: when a fire truck passes an observer, the pitch of the siren is higher when approaching the observer, while after passing the observer, the pitch is lower. This phenomenon also applies to light as electromagnetic waves: If the matter that is emitting light approaches, its light is compressed, and therefore appears shifted toward the blue part of the spectrum. On the other hand, if the emitter recedes, the light is stretched, and appears to be shifted toward the red part of the spectrum. This effect also applies to absorption of light, and is crucial when dealing with very high velocities, as encountered in the astronomical or astrophysical context. Astrophysicists perform 3D simulations of scenarios, like the evolution of galaxies or the merger of black holes, to predict and study their behavior—and physically relevant visualizations need to take the Doppler effect into account.

To be able to account for the Doppler effect, spectral volume rendering requires the use of a spectral model of light. As discussed below, spectral volume rendering aims to address the shortcomings of RGB color models, by assigning spectra to the input data, and using spectral representation throughout the rendering process in order to obtain accurate results. In the case of astrophysical data, light radiance comes from matter, both as thermal radiation or by free charged particle acceleration, respectively, and every volume element can emit and absorb light of any frequencies of the spectrum. Moreover, the velocity within each volume element needs to be considered for computing how the electromagnetic waves are modified by the Doppler effect along the line of sight. This translates into shift operations in the spectrum while compositing the spectra of each sample during ray casting.

To represent light spectra in volume rendering, the simplest approach is to point-sample the spectrum at uniform intervals, dividing the spectrum into a number of frequency bands. Since a spectrum describes the power of the emitted light frequency, spectra can simply be added to obtain the result of multiple light emissions. The light–matter interaction in the case of such a spectral representation can be determined by multiplying the spectrum of the incident light with the reflection or absorption spectrum of the medium, resulting in the spectrum of the outgoing light. The reflectance and absorption functions describe how much of the incident light is reflected and transmitted, at each wavelength. Thus, these operations can be performed for each frequency band in the discretized approach.

However, as we will show, employing the Doppler effect using point-sampled representation of spectra has several drawbacks: First, matter emits light in very thin, specific frequencies called *spectral lines*. Thus, applying the Doppler effect and discretizing the result into bins results in inaccuracies regarding the conservation of energy. Also, a single absorption line then affects all the energy within the interval of a given bin. Moreover, if the bin range is not large enough, e.g., when dealing only with the visible spectrum, information can be lost when emission/absorption computations shift from the visible into the invisible spectrum, and vice

versa. Finally, since velocities vary continuously from sample to sample evaluated along a ray, spectral lines which are being emitted within an interval of line of sight are shifted by different amounts, resulting in spectral broadening. This means that spectral lines become continuous bands due to the Doppler effect. The widely employed assumption that the velocity is constant along a ray segment does often not hold and violates the involved physical effects. Some of these problems could be partially solved by increasing the sampling rate along rays, and by increasing the number of bins in the spectrum range considered. However, as we show in this paper, this approach exponentially increases the complexity of the evaluation of each ray, and thus makes it impossible to obtain interactive frame rates. For these reasons, we propose a novel representation of light spectra based on dynamically computed and combined piecewise linear segments. Our approach supports precise Doppler shifts with moderate additional complexity to the volume rendering process.

The main contributions of this paper are:

- The adaptation of spectral volume rendering for a per-voxel emission/absorption scheme, with both thermal radiation (black-body emission) and photon generation by free charged particles.
- The first accurate Doppler effect computation in volume rendering, corresponding to the motion given by a 3D velocity field.
- A novel dynamic, piecewise linear representation of light spectra that is tailored to the implications of the Doppler effect, overcoming the drawbacks of point-sampled spectral representations.
- An interactive GPU volume renderer for the proposed techniques, and its application to a simulation of galaxy formation.

## 2. Related Work

Visualization of 3D volumes is often achieved using ray casting processed on the GPU [HLSR09]. Spectral volume rendering for more advanced optical effects was first introduced by Noordmans et al. [NvdVS00], who modified the existing rendering methods to obtain a spectral model. For that, they represented spectra by point samples, making the extension from a three-channel accumulation to an  $n$ -channel one straightforward. They also rewrote the volume rendering integral to a spectral form. In their approach, light comes from an outside source that emits light with a set of spectral distribution functions. Light that is reflected by the volume is determined by the reflection spectra of the materials inside. A similar spectral model was adopted by Bergner et al. [BMDF02], who made use of spectral phenomena to create new means of exploring volumetric data. They adapted a linear color model, which allows for quick re-illumination of the scene as a post-processing step [BMTD05]. However, this is only possible if the light source is external, i.e., not part of the volume. A representation of spectra more advanced than binning was presented by Raso and Fournier [RF91] using piecewise polynomials. Later on, Peercy [Pee93] proposed a linear color model using general basis functions. This was later improved by Finlayson et al. [FDF94], who used spectral sharpening, a technique from digital photography to simplify spectral calculations. This way, a major speedup could be achieved, since it reduces the large number of samples that have to be processed to a handful of coefficients. A hybrid representation was explored by Sun et al. [SFDC01] to compensate for the issues that point-sampled

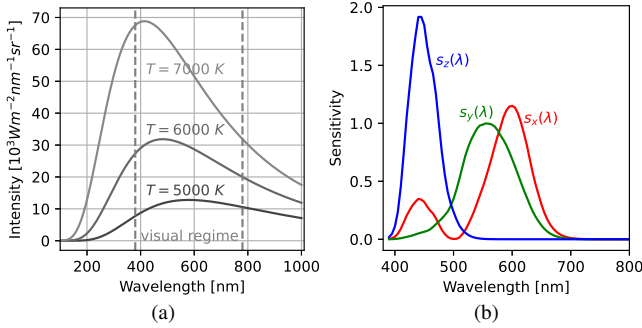


**Figure 2:** (a) Black-body spectra  $B(T, \lambda)$  according to Equation 1. The maximum shifts toward the blue part of the spectrum for higher temperatures. (b) CIE XYZ color matching functions represent the average sensitivity of the human eyes with respect to X, Y, and Z.

spectra and smooth function fitting have. Other spectral rendering models have made use of the Kubelka–Monk theory to explicitly model the appearance of materials and provide color realism. Abdul-Rahman and Chen [ARC05] presented a one-dimensional radiosity algorithm based on this theory, and model two directions of light flux along viewing rays. Strengert et al. [SKB\*06] implemented spectral ray casting on the GPU.

The Doppler effect has been studied in relativistic visualizations by Weiskopf et al. [WKR99], but only for non-interactive ray tracing of meshes. Other tools for 3D astrophysical modeling use the Doppler effect for correcting the geometry of astronomic objects [SKW\*10], but not for simulating it. Our framework represents the first accurate Doppler effect computation in interactive volume rendering, corresponding to the motion given by a 3D velocity field. Complementary to our approach, the visualization of 3D integral field spectroscopy (IFS) data, which consists of two spatial and one spectral dimensions, was accomplished using standard 3D rendering techniques by Boussejra et al. [BUT\*19] and Uchiki et al. [UBZ\*20].

For improved depth perception and also in the astrophysical context, Ament et al. introduced ambient volume scattering [ASW13] and volumetric shadows [ASDW14]. Such global illumination models could be easily extended with our framework to include the Doppler effect in the involved light distribution and light collection phases. Likewise, most traditional and abovementioned spectral volume rendering techniques could be extended with the Doppler effect using our framework, since it can represent arbitrary spectra.

### 3. Theoretical Background

Let us first introduce the main formulations of electromagnetic radiation, as required by our volume rendering approach.

#### 3.1. Physics of Light

There are many ways in which matter can emit electromagnetic radiation. Two of the most important are thermal radiation, and radiation from free charged particle acceleration. The radiation of a thermal source can be approximated by the continuous spectrum

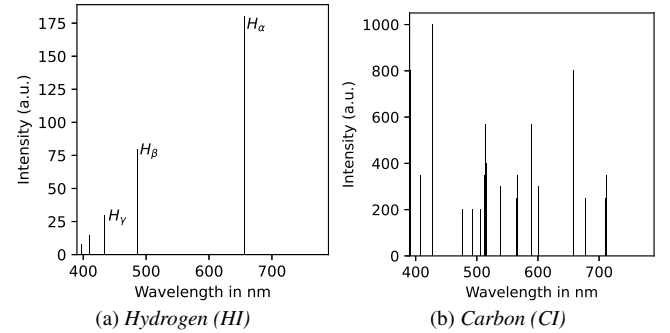


**Figure 3:** Line spectra for hydrogen (a) and carbon (b) in the visual domain. The HI-spectrum shows typical Balmer series  $H_\alpha$ ,  $H_\beta$ , etc.

of an idealized black-body. The spectral distribution function expressed per unit wavelength  $\lambda$  is given by Planck's radiation law

$$B_\lambda(T, \lambda) = \frac{2hc^2}{\lambda^5} \left[ \exp\left(\frac{hc}{\lambda k_B T}\right) - 1 \right]^{-1}, \quad (1)$$

with Planck's constant  $h$ , Boltzmann's constant  $k_B$ , speed of light  $c$ , and temperature  $T$ . See, e.g., Karttunen et al. [K\*17] for more details. Figure 2a shows Planck spectra for different temperatures. The maximum of  $B_\lambda(T, \lambda)$  for a given temperature is given by Wien's displacement law

$$\lambda_{\max} = 2.897 \times 10^{-3} \text{ m K}/T. \quad (2)$$

As an example, the spectrum of our Sun can be approximated by a black-body with an effective temperature of  $T \approx 5770 \text{ K}$  and a maximum at  $\lambda_{\max} \approx 502 \text{ nm}$  with corresponding spectral radians  $B(T, \lambda_{\max}) \approx 26.2 \text{ kW m}^{-2} \text{ nm}^{-1} \text{ sr}^{-1}$ .

On the other hand, non-thermal radiation can be described by individual spectral lines which are due to energy transitions in atoms or molecules. Figure 3a shows the spectral lines of neutral hydrogen (HI) in the visual regime also called Balmer lines, and Figure 3b for carbon (CI).

When a light wave passes through matter, it is typically subject to a decrease in intensity. This attenuation is described by the Lambert–Bouguer law, which states that the portion of transmitted light is dependent on the density  $\rho$  of the material, the thickness  $l$  of the sample, and the extinction coefficient  $\tau$  for wavelength  $\lambda$ :

$$I(\lambda) = I_0(\lambda) e^{-l\rho\tau(\lambda)}. \quad (3)$$

Spectral lines can be observed either as emission or absorption lines. However, idealized delta-peak-like spectral lines, as shown in Figure 3, will never appear in nature due to various line broadening effects. These include, for example, thermal Doppler broadening due to the distribution of velocities in a gas, or pressure broadening.

#### 3.2. Doppler Effect

The Doppler effect is a familiar phenomenon from everyday life, when a sound emitter drives by and the sound changes from higher to lower tones. This is because the wavelengths of the sound waves are either compressed or stretched. A similar effect happens with

light, when a light source approaches the observer, or vice versa. Here, however, much higher velocities close to the speed of light are required to achieve a direct visual effect. If wavelengths are compressed to shorter ones, this is called blue-shift, whereas, if they are stretched to longer ones, it is called red-shift.

Exact calculations within the framework of the special relativity theory yields the transformation equation of wavelengths  $\lambda \mapsto \lambda'$ :

$$\frac{\lambda'}{\lambda} = \gamma [1 - \beta \cos(\chi')], \quad (4)$$

with scaled velocity  $\beta = v/c$ , velocity magnitude  $v$ , wavelength  $\lambda$ , gamma factor  $\gamma = 1/\sqrt{1 - \beta^2}$ , and  $\chi'$  being the angle between the incoming light ray and the direction of motion, see, e.g., [Rin04].

The Doppler shift of a black-body spectrum is again a black-body spectrum, but at a different temperature. This can be deduced from the relativistic Liouville theorem that states that  $B_V/v^3 \equiv \text{const.}$ , where  $B_V$  is the Planck's radiation law with respect to frequency  $v = c/\lambda$ . Then, the observed temperature  $T_{\text{obs}}$  follows from the emitted temperature  $T_{\text{emit}}$  via [MTW73]

$$\frac{T_{\text{obs}}}{T_{\text{emit}}} = \frac{\lambda_{\text{emit}}}{\lambda_{\text{obs}}}. \quad (5)$$

However, to simplify calculations, we use the following approximation for low velocities

$$\lambda' = \lambda \left(1 + \frac{v_r}{c}\right), \quad (6)$$

where  $v_r$  is the radial component along the viewing direction. Thus, we ignore any tangential components. Positive values of  $v_r$  result in larger wavelengths (red-shift), whereas negative values result in smaller wavelengths (blue-shift). The Doppler shift for a black-body spectrum is simplified similarly as:

$$T' = T \left(1 - \frac{v_r}{c}\right). \quad (7)$$

Therefore, black-body radiation appears cooler for objects that are moving away, and hotter for objects that are getting closer.

### 3.3. Spectral Representation

To represent spectra in a rendering application, the simplest method is to point-sample the spectrum at uniform intervals, effectively dividing the spectrum into a number of bands. When accumulating emission and absorption along viewing rays, we would need to do so for every band of the sampled spectrum separately. Spectral distribution functions can be simply added together due to the additive nature of spectral radiance. The traditional volume rendering integral is then expanded to generalize the emission and absorption model, and must be evaluated for every wavelength:

$$I(s + \Delta s, \lambda) = \sum_{m=1}^M \rho_m(s) E_m(\lambda) + I(s, \lambda) \left(1 - \Delta s \sum_{m=1}^M \rho_m(s) A_m(\lambda)\right). \quad (8)$$

Here,  $I(s + \Delta s, \lambda)$  is the intensity at the next integration step, as the sum of the total emission of all materials and the intensity of the incoming light flux  $I(s, \lambda)$ .  $E_m(\lambda)$  denotes the emitted power of

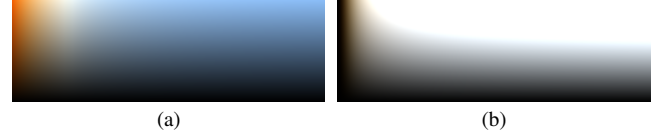


**Figure 4:** Color tables for Planck spectra from  $T_{\min} = 1000\text{ K}$  to  $T_{\max} = 26\,000\text{ K}$  (horizontal axis, left to right) scaled by the luminance  $Y$  for each temperature (a) or by the luminance for  $T = 1500\text{ K}$  (b). The vertical axis scales  $C_{sRGB}$  by a factor  $f \in [0, 1]$ .

material  $m$  at wavelength  $\lambda$ , and corresponds to the spectral distribution function of that material. Similarly,  $A_m(\lambda)$  is the absorption of material  $m$  at wavelength  $\lambda$ .

### 3.4. Spectrum Convolution to RGB Color

Given a spectral intensity distribution  $I(\lambda)$ , we can determine the visual perception in three steps (see, e.g., Wyszecki and Stiles [WS00]). First, we calculate the CIE XYZ tristimulus values  $X_i = \{X, Y, Z\}$  from the sensitivity functions  $s_i = \{s_x(\lambda), s_y(\lambda), s_z(\lambda)\}$  (Figure 2b) via the convolution integral

$$X_i = \int_{\lambda_{\min}}^{\lambda_{\max}} I(\lambda) s_i(\lambda) d\lambda. \quad (9)$$

Then, we convert these XYZ values to linear RGB color space using the following transformation matrix [Lin]

$$\begin{bmatrix} R_{\text{lin}} \\ G_{\text{lin}} \\ B_{\text{lin}} \end{bmatrix} = \begin{bmatrix} 2.37067 & -0.90004 & -0.47063 \\ -0.51389 & 1.42530 & 0.08858 \\ 0.00530 & -0.01470 & 1.00940 \end{bmatrix} \begin{bmatrix} X \\ Y \\ Z \end{bmatrix}. \quad (10)$$

The final transformation to sRGB space is given by

$$C_{sRGB} = \begin{cases} 12.92C_{\text{lin}}, & C_{\text{lin}} \leq 0.0031308 \\ (1+a)C_{\text{lin}}^{1/2.4} - a, & C_{\text{lin}} > 0.0031308 \end{cases}, \quad (11)$$

where  $a = 0.055$  and  $C_{\text{lin}} = \{R_{\text{lin}}, G_{\text{lin}}, B_{\text{lin}}\}$ . However, without any modifications, this would map all temperatures below 1900K to yellow, and the others to white due to gamut restrictions. Hence, we scale the tristimulus values either individually or by a constant factor before mapping them to the sRGB color space, see Figure 4.

## 4. Method

Before presenting the novel concept of piecewise linear spectra, we first discuss the limitations of the traditional approach in the application of the Doppler effect.

### 4.1. Point-Sampled Spectrum Model

The simplest method to represent spectra is to point-sample them at uniform intervals, i.e., dividing the spectrum into  $N$  bands (see, e.g., Figure 5). However, this representation has a number of limitations:

- **Loss of energy conservation.** Spectral distribution functions can be simply added due to the additive nature of spectral radiance. We may approximate the transmittance term  $e^{-l\rho\tau(\lambda)}$  of Equation 3 by linearization to obtain  $1 - l\rho\tau(\lambda)$ . However, this only

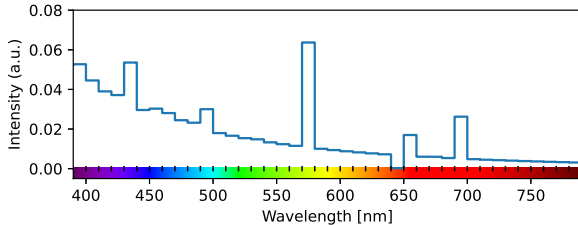


**Figure 5:** Example spectrum with  $N = 40$  fixed bands in the visual domain  $\lambda \in [390, 780]$  nm.

holds when assuming sufficiently small thickness. This means that, when dealing with high extinctions or densities, the step size has to be sufficiently small, or it will lead to amplification of the incident light instead of an attenuation.

- **Loss of information.** When applying the Doppler effect, light intensities can be shifted out of the range of considered bands.
- **Loss of accuracy.** Figure 6 illustrates the Doppler shift of a single spectral line. While the spectral line is just a  $\delta$ -peak at  $\lambda_e$ , it converts into a rectangle of width  $\Delta\lambda$  at  $\lambda_3$  in the fixed bands representation. A Doppler shift of this band with Doppler factor  $D$  yields  $\lambda'_3 = D\lambda_3$ . If  $\lambda'_3$  is still in the  $\lambda_3$  band, there is effectively no Doppler shift. On the other hand, if  $\lambda'_3$  falls into another band, the Doppler shift could be either over- or underestimated. In the next integration step, not  $\lambda'_3$  but  $\lambda_2$  would be used for calculating the Doppler shift. Furthermore, this could lead to apparent emission or absorption lines, as illustrated in Figure 7.
- **The Doppler effect is discrete and depends on  $N$ .** As a consequence of the previous point, the effective visual influence of the Doppler effect will depend on  $N$ : given the Doppler factor  $D = 1 + v/c$ , the number of bands  $N$ , and the width of the bands  $\Delta\lambda = (\lambda_{\max} - \lambda_{\min})/N$ , then, the minimum velocity that has a visual influence follows from:  $\lambda' = D\lambda$ ,  $\lambda + \Delta\lambda/2 = D\lambda$ ,  $D = 1 + \Delta\lambda/(2\lambda)$ . For example, if  $N = 40$ ,  $\lambda \in [390, 790]$ ,  $\Delta\lambda = 10$ ,  $\lambda = 390 \Rightarrow v/c \approx 0.0128$ ,  $\lambda = 790 \Rightarrow v/c \approx 0.0063$ .
- **Not representing broadening.** The Doppler effect leads to line broadening. That is why single spectral lines ( $\delta$ -peaks) will never be observed in nature. A fixed band representation cannot reproduce this effect.

To tackle these problems, an immediate solution could consist of using a very high number of bands and dynamic adaptation of the represented range. However, in practice, this would increase the required amount of computation drastically, as we show in Section 6.

#### 4.2. Piecewise Linear Spectrum Model

To ensure that the above issues are addressed, we move away from binning and sampling the spectrum, and substitute a continuous spectrum representation for the discrete model. Spectral lines and bands shall be represented by their exact position in the spectrum and the correct intensity at each point in that band. For this model to be computationally feasible, we assume that the scalar densities, as well as the velocities and their respective projected portion, vary linearly in between two sample points along a viewing ray. This idea is analogous to the one from pre-integration [EKE01], where the scalar values are assumed to vary linearly along segments of the

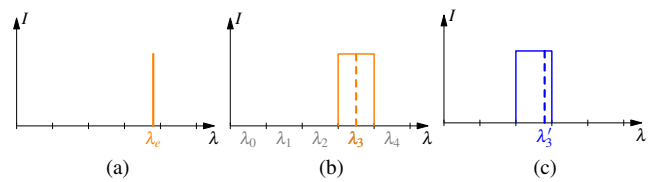


**Figure 6:** From single spectral line  $\lambda_e$  (a), to band representation  $\lambda_3$  (b), to Doppler-shifted wavelength  $\lambda'_3 = D\lambda_3$  (c) with  $D < 1$ .

ray. As in the case of pre-integration, the assumption that the density, and in our case also the velocity, vary linearly along a ray segment holds for tensor-product linear interpolation only for parallel projection, when the viewing rays align with one of the parametric axes. Such linearity assumption has also practical advantages, since graphics hardware implements linear interpolation natively, providing respective acceleration. In the case of non-axis-aligned views, we follow the pre-integration approach [EKE01] by still assuming linear variation along the ray segments to keep our model computationally feasible. In such cases, the linearity assumption is still appropriate for sufficiently small step sizes. In addition, through linearly varying density along a ray segment, the intensity of emitted light is also varying linearly. Furthermore, in our case, the velocity is varying linearly too, which means that waves emitted by the segment are shifted due to the velocities that appear on the segment. This leads to the possibility of modeling spectral broadening, where the velocity has to vary continuously.

**Model.** A spectral line that is emitted by particles in between two sample points along a viewing ray is shifted differently by every velocity between those sample points. This results in a continuous band due to spectral broadening. Additionally, the density at those sample points varies linearly, meaning the emitted band has a linearly varying intensity. Therefore, a line is broadened to a band that takes the shape of a trapezoid (Figure 9), described by

$$f(x) = \begin{cases} mx + b, & x_{\min} \leq x \leq x_{\max} \\ 0, & \text{else} \end{cases}, \quad (12)$$

with start  $x_{\min}$  and endpoint  $x_{\max}$  of the band. Then, a spectrum  $S(\lambda)$  can be described as piecewise linear function of the form

$$S(\lambda) = \sum_{i=1}^N (m_i \lambda + b_i) \mathbb{1}_{[\lambda_{i,\min}, \lambda_{i,\max}]}(\lambda), \quad (13)$$

with indicator function  $\mathbb{1}_{\mathcal{A}}(x)$  for the contiguous set  $\mathcal{A}$ ,

$$\mathbb{1}_{\mathcal{A}}(x) = \begin{cases} 1, & x \in \mathcal{A} \\ 0, & x \notin \mathcal{A} \end{cases}. \quad (14)$$

It is important to note that the pieces are strictly nonnegative in their defined intervals, since there is no negative spectral intensity. Furthermore, the intervals  $\mathcal{A}_i$  may not overlap.

**Accumulation.** Before the spectra can be accumulated along a viewing ray, the spectral lines first are broadened into their trapezoidal shape. Since intervals are not uniform, because every band has its own position and width, the accumulation becomes more complicated compared to point-sampled spectra. Linear pieces that are defined on overlapping intervals have to be split into new pieces,

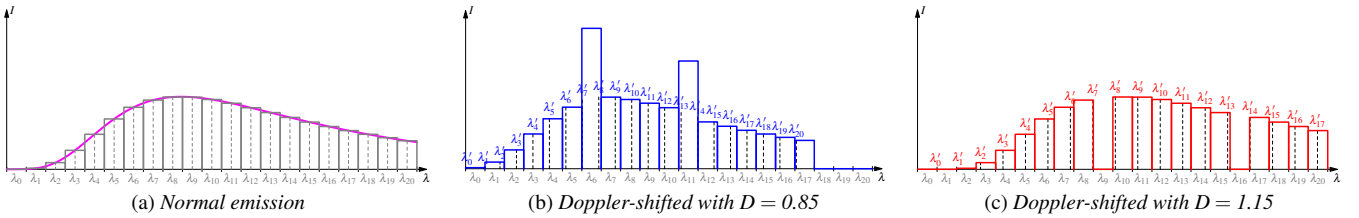


**Figure 7:** Sample-based black-body spectra examples in the domain  $\lambda \in [100, 1000]$  nm for  $T = 6000$  K and  $N = 21$  bands. (b) Blue-shift with  $D = 0.85$  leads to apparent emission lines at  $\lambda_6$  and  $\lambda_{11}$ . (c) Red-shift with  $D = 1.15$  leads to apparent absorption lines at  $\lambda_9$  and  $\lambda_{16}$ .

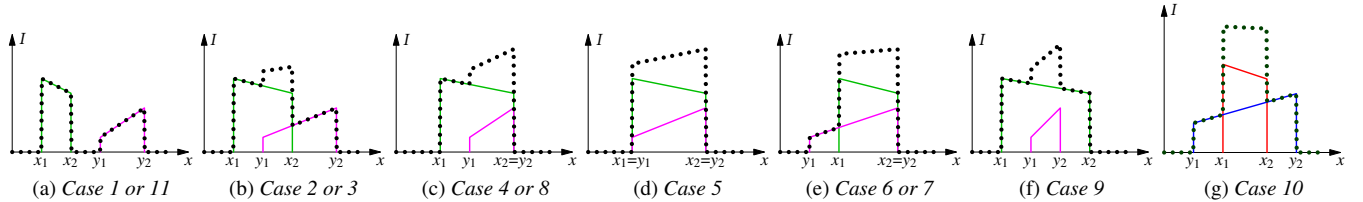


**Figure 8:** All cases of accumulating two linear functions, with (1) the linear function shown in green defined in the interval  $[x_1, x_2]$ , and (2) the linear function shown in magenta defined in the interval  $[y_1, y_2]$ . The resulting sum of both functions is indicated by the dotted line.

and added together appropriately, refining the whole spectral function in this process. Figure 8 shows the situation for the two piecewise linear functions  $f(x)$  and  $g(x)$ , described by Equation 12. There is a total of 11 cases of how two intervals can be related to each other, and eight of them lead to fragmentation into up to three new intervals. They are detailed in the supplemental material accompanying this work. Since the compositing scheme is complicated and highly recursive due to the potentially repetitive splitting of the intervals, it is expected to be typically the most time-consuming part of the rendering process.

Figure 9 illustrates different aspects of the piecewise linear function: (a) shows a line spectrum consisting of two delta peaks at wavelengths  $\lambda_a$  and  $\lambda_b$ . Because delta peaks are not realistic in nature, they will be approximated by box functions of limited width  $\delta\lambda$  (b). The plots in the middle row of Figure 9 show the situation for the two spectral lines for the first three integration steps: density  $\rho$  and radial velocities  $v_r$  change along the viewing ray as  $\rho = [1.0, 1.4, 1.2, 1.1]$  and  $v_r = [-0.3, -0.4, -0.5, -0.25]$ . Because  $v_r$  is always negative, the spectral lines will be all blue-shifted to smaller wavelengths. In the first step (c), both spectral lines will be shifted due to  $v_r = -0.3$  and  $v_r = -0.4$  with density factors  $\rho = 1.0$  and  $\rho = 1.4$ , respectively, which yields the two trapezoids. In the second step (d), the spectral lines will be shifted due to  $v_r = -0.4$  and  $v_r = -0.5$  with density factors  $\rho = 1.4$  and  $\rho = 1.2$ . In the same way, step three (e) follows. Figure 9f shows the combination of all three steps which are then fragmented into new intervals and summed up, as shown in (g).

During the accumulation, it may happen that a new trapezoid needs to be created next to an existing one. In such a case, we can merge both trapezoids if they are close enough and they have similar slopes. These situations often occur due to the broadening, and this clustering helps to keep the number of trapezoids of the spectra low. A threshold controls this process, which allows being stricter or looser in the conditions of merging.

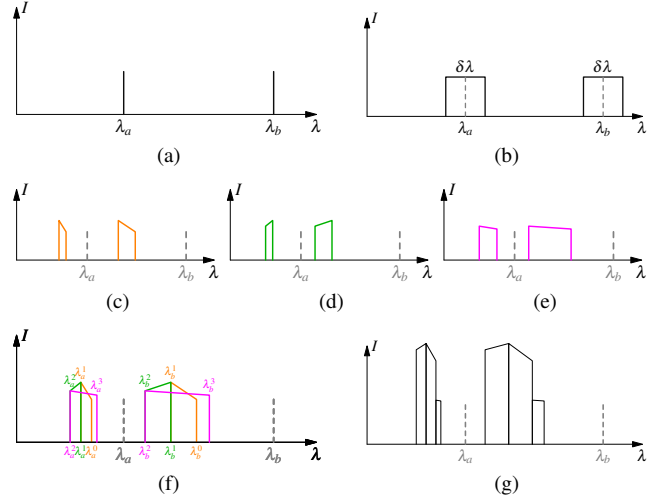


**Figure 9:** Example of representation, accumulation, and convolution of a spectrum consisting of two spectral lines, represented with the proposed piecewise linear basis functions.

**Convolution.** Once the final spectrum is calculated, the observed color has to be determined for a given sensitivity function (observer). In order to obtain this color, the integrals in Equation 9 have to be evaluated, as in the point-sampled model. However, with our approach, we solve the integration more accurately and avoid the use of discrete Riemann integration. To represent the sensor function more accurately, we model it as a piecewise linear function too, instead of assuming it to be piecewise constant. Thus, the convolution of the resulting spectrum and the CIE matching functions can be performed analytically for each piece. For this, it is important to use the correct boundaries for the integration, since the two pieces may overlap only partially. For two piecewise linear functions, as

**Algorithm 1** Ray integration using fixed bands.

---

```

Require: bands[NBANDS]
while ray inside volume do
    fetch velocity v
    DOPPLER_FACTOR  $\leftarrow v/c$ 
    fetch density  $\rho$ , temperature T
     $T \leftarrow T * (1 + DOPPLER\_FACTOR)$ 
    for each band b do
         $\lambda \leftarrow (390 + b * \Delta\lambda) * 1e-9$ 
        bands[b]  $\leftarrow$  bands[b]  $+ \rho * \text{PLANCKLAW}(\lambda, T)$ 
    end for
    for each material m do
        fetch density  $\rho$ 
        for each every band b do
             $\lambda \leftarrow (390 + b * \Delta\lambda) * 1e-9$ 
             $\lambda \leftarrow \lambda * (1 - DOPPLER\_FACTOR)$ 
            new_b  $\leftarrow (\lambda - 390) / (\Delta\lambda)$ 
            bands[new_b]  $\leftarrow$  bands[new_b]  $+ \rho * \text{emissionSpect[m][b]}$ 
            bands[new_b]  $\leftarrow$  bands[new_b]  $- \rho * \text{absorptionSpect[m][b]}$ 
        end for
    end for
end while
xyz  $\leftarrow \text{SPECTRUMTOXYZ}(\text{bands})$ 
rgb  $\leftarrow \text{XYZTORGB}(xyz)$ 

```

---

in Equation 12, where  $f(x)$  represents part of the spectrum and  $g(x)$  represents part of the CIE matching function, we obtain

$$\begin{aligned}
& \int_{-\infty}^{\infty} f(x)g(x)dx \\
&= \int_{-\infty}^{\infty} (m_1x + b_1)(m_2x + b_2) \mathbb{1}_{\{x_1 \leq x \leq x_2\}} \mathbb{1}_{\{y_1 \leq x \leq y_2\}} dx \\
&= \int_{\max(x_1, y_1)}^{\min(x_2, y_2)} m_1 m_2 x^2 + (m_1 b_2 + m_2 b_1)x + b_1 b_2 dx \\
&= \left[ \frac{1}{3} m_1 m_2 x^3 + \frac{1}{2} (m_1 b_2 + m_2 b_1) x^2 + b_1 b_2 x \right]_{\max(x_1, y_1)}^{\min(x_2, y_2)}.
\end{aligned}$$

The final color is obtained by evaluating the integral for every piece in the spectrum with every piece of the sensor that lies in the former's interval, and by summing up these contributions. The resulting color is an XYZ triplet, which can in turn be converted into an RGB color by multiplication with a suitable transformation matrix, like the one in Equation 10.

## 5. Implementation

We have implemented an interactive GPU spectral ray casting volume renderer using CUDA and OpenGL, supporting both spectral representations and operations. The renderer supports the emission models described in Section 3. The black-body emission is computed analytically on-the-fly by using Planck's law and the temperature scalar field. For the matter emission, the spectral lines of each element are stored in local GPU memory. It proceeds by shooting rays through the pixels of the screen and sampling the data, computing the emission and absorption, and accumulating the resultant spectrum. Once a ray has exited the volume, the spectrum is convolved with the CIE functions to calculate XYZ color, which is then used to calculate the corresponding RGB value, by tables stored in local GPU memory. The tool is interactive and supports

picking pixels to inspect their spectra, as well as simulating a step-by-step accumulation evolution of a single ray through the volume (as shown in the accompanying video), which allows to better understand how the final spectrum is achieved. Also, scaling factors of the data (temperature, density, etc.) are included for controlling the final result of the visualization and for highlighting the effects of the Doppler effect. The virtual observer camera is expected to be quasi-static. Hence, any camera motion of the user is not taken into account, but only the radial velocities of the data components. As the magnitudes we deal with are extreme, we use double-precision floating point numbers for the computations. The entire dataset is loaded to global GPU memory as 3D textures, and samples are fetched on demand using trilinear interpolation. Our implementation could be potentially scaled for larger datasets by using common techniques for large volume visualization, such as texture compression [RGG\*13] or out-of-core rendering [FK10].

**Doppler rendering with fixed bands.** For the point-sampled approach, the spectra are divided into bands of equal width, implemented with a configurable, fixed number  $N$  of bins, as described in Section 4.1. In this case, black-body accumulation simply follows Planck's law (Equation 1), and is applied using  $\lambda_i$  and temperature multiplied by the Doppler factor. The resulting intensity is multiplied by density. For the line emission of the materials, the spectrum at  $\lambda_i$  times the Doppler correction has the same intensity as the line emission spectrum at position  $\lambda_i$  multiplied by the element's density. Apart from the common outer loops (iteration of pixels and samples), the complexity of the algorithm (which is shown in Algorithm 1) is mainly characterized by the number of spectral bands.

**Doppler rendering with piecewise linear functions.** The second (and main) version implements our new piecewise linear function representation of spectra, and the accumulation and convolution steps described in Section 4.2. Thus, the spectrum is represented as lines with start/end positions, slope, and intercept. In this case, when using the black-body emission, for each  $\lambda_i$  piece in the visible spectrum, the two intensity values are calculated by applying Planck's law (Equation 1) twice: once using the first sample, and then using the second sample. The slope and intercept are calculated, and the new linear piece is added to the spectrum. The old samples are assigned the value of the new samples for the next volume rendering loop. When dealing with line emission, for each delta peak of each material  $x_1$  and  $x_2$ , we evaluate  $\lambda_i \pm \varepsilon$  multiplied by the Doppler factor of the first and second samples, respectively. The new trapezoid is added to the piecewise linear function, by employing the cases from Figure 8. In this case, the complexity of the algorithm (Algorithm 2) mainly depends on the (fixed) number of samples used for describing the black-body emission (as shown in Figure 10, 21 turned out to provide a very good description of the curve) and the number of delta peaks of the materials.

## 6. Results and Discussion

**Dataset.** We applied our method to a real astronomical dataset, described by Sormani et al. [STR\*18], which simulates the asymmetries in the innermost region of the Milky Way, the Central Molecular Zone (CMZ). They showed that this asymmetry can be explained by unsteady flow of gas in a barred potential. For that, they

**Algorithm 2** Ray integration using piecewise linear function.

```

fetch velocity  $v_1$ , density  $\rho_1$ , temperature  $T_1$ 
for every material m do
    fetch density  $\rho_m$ 
end for
while ray inside volume do
    fetch velocity  $v_2$ 
    DOPPLER_FACTOR_1  $\leftarrow v_1/C$ 
    DOPPLER_FACTOR_2  $\leftarrow v_2/C$ 
    fetch density  $\rho_2$ , temperature  $T_2$ 
     $T_1 \leftarrow T_1 * (1 + \text{DOPPLER\_FACTOR\_1})$ 
     $T_2 \leftarrow T_2 * (1 + \text{DOPPLER\_FACTOR\_2})$ 
    for each band b do
         $x_1 \leftarrow (390 + b * \Delta\lambda) * 1e-9$ 
         $x_2 \leftarrow (390 + (b + 1) * \Delta\lambda) * 1e-9$ 
         $y_1 \leftarrow \rho_1 * \text{PLANCKLAW}(x_1, T_1)$ 
         $y_2 \leftarrow \rho_2 * \text{PLANCKLAW}(x_2, T_2)$ 
        ADDBANDTOSPECTRUM( $x_1, x_2, y_1, y_2$ )
    end for
     $T_1 \leftarrow T_2$ 
     $\rho_1 \leftarrow \rho_2$ 
    for each material m do
        fetch density  $\rho_m$ 
        for each  $\lambda$ , intensity in emissionSpectrum[m] do
             $x_1 \leftarrow (\lambda - \epsilon) * (1 - \text{DOPPLER\_FACTOR\_1})$ 
             $x_2 \leftarrow (\lambda + \epsilon) * (1 - \text{DOPPLER\_FACTOR\_2})$ 
             $y_1 \leftarrow \rho_{m1} * \text{intensity}$ 
             $y_2 \leftarrow \rho_{m2} * \text{intensity}$ 
            ADDPIECEtospectrum( $x_1, x_2, y_1, y_2$ )
        end for
        for each  $\lambda$ , intensity in absorptionSpectrum[m] do
             $x_1 \leftarrow (\lambda - \epsilon) * (1 - \text{DOPPLER\_FACTOR\_1})$ 
             $x_2 \leftarrow (\lambda + \epsilon) * (1 - \text{DOPPLER\_FACTOR\_2})$ 
             $y_1 \leftarrow -\rho_{m1} * \text{intensity}$ 
             $y_2 \leftarrow -\rho_{m2} * \text{intensity}$ 
            ADDPIECEtospectrum( $x_1, x_2, y_1, y_2$ )
        end for
         $\rho_{m1} \leftarrow \rho_{m2}$ 
    end for
     $v_1 \leftarrow v_2$ 
end while
xyz  $\leftarrow \text{CONVOLVESPECTRUM}()$ 
rgb  $\leftarrow \text{XYZTORGB}(xyz)$ 

```

used a high-resolution 3D hydrodynamical simulation with no self-gravity of gas but including chemical reactions that make the gas subject to thermal instabilities. The simulation was based on the moving mesh code AREPO by Springel [Spr10]. For our purposes, we resampled the data onto a uniform grid of size  $128^3$ . In doing that, for the sake of clear visualization, we stretch the  $z$ -axis to get a cubical volume. The data consist of a set of scalar fields, including dust density, emitting matter temperature, matter densities of hydrogen, helium, and carbon, as well as a velocity vector field. Figure 11 shows vertical slices of some of these variables. More details about the ranges and magnitudes of this dataset can be consulted in the supplemental material included with this document.

**Input parameters.** Our technique takes as input the dataset described, together with descriptors of the emission lines of the different kinds of matter. For our experiments, those emission spectra were provided together with the galaxy simulation, but they could also be selected by the user, e.g., from the Astronomic Spectra Database [KYRa17]. The amount of energy radiated by the matter scales the intensity of those spectral lines by the density of the matter defined in the dataset. At runtime, the user can modify multipliers for different parameters of the dataset: velocity magnitude, temperature, and intensity of the light emission and absorption, in order to highlight the impact of the Doppler effect, if required.

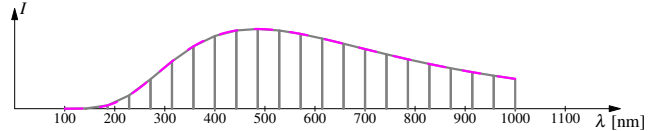


**Figure 10:** Black-body spectrum approximated with our piecewise linear function. Due to the slopes of the trapezoids, the curve can be approximated with just 21 segments.

**Test system.** All experiments were performed on a PC with Intel Xeon processor and 128 GB of main memory, running Ubuntu 20.04 OS. The graphics card was a NVidia Titan RTX with 24 GB of memory. Our prototype was written in C++, using CUDA 10.1 and OpenGL 4.6.

**Correctness and accuracy.** First, for validating the correct behavior of the proposed method, we used different setups of synthetic data. The one in Figure 12 consists of a radial density field of hydrogen, moved by a vector field with a spherical shape, of a thickness around 10% of the side of the volume. The figure shows two sample spectra along respective rays traversing the velocity field. At  $s1$ , it can be observed how the spectrum shifts toward lower wavelengths (blue-shift), and how it is broadened as a consequence of the different vector velocities. The same effect can be observed at  $s2$ , in the opposite direction (red-shift), as expected. We claim that our method provides a ground truth when rendering a volume with the viewing rays aligned with one of the Cartesian axes of the dataset. To support this, we show in Figure 13 that increasing the number of samples in a spectrum makes the resulting images converge to the ones produced by our method, but requiring much higher rendering times.

**Performance.** Table 1 shows the frame render times for the images provided in Figures 12 and 14 to 17, as well as the used factors. First, it is remarkable that the black-body emission does not

**Table 1:** Rendering times and factors for selected result figures.

	Doppler effect	Render time (ms)	Velocity factor	Temp. factor
Figure 12 synthetic	—	95	$5 \times 10^7$	—
	✓	278	$5 \times 10^7$	—
Figure 14 black-body	—	84	200	15
	✓	91	200	15
Figure 15 hydrogen	—	561	200	—
	✓	1190	200	—
Figure 16 BB & HI & CO	—	3845	200	15
	✓	16751	200	15
Figure 17 HI & CO & He (Merge tol. = $1e^{-3}$ )	—	3523	80	—
	✓	78933	80	—

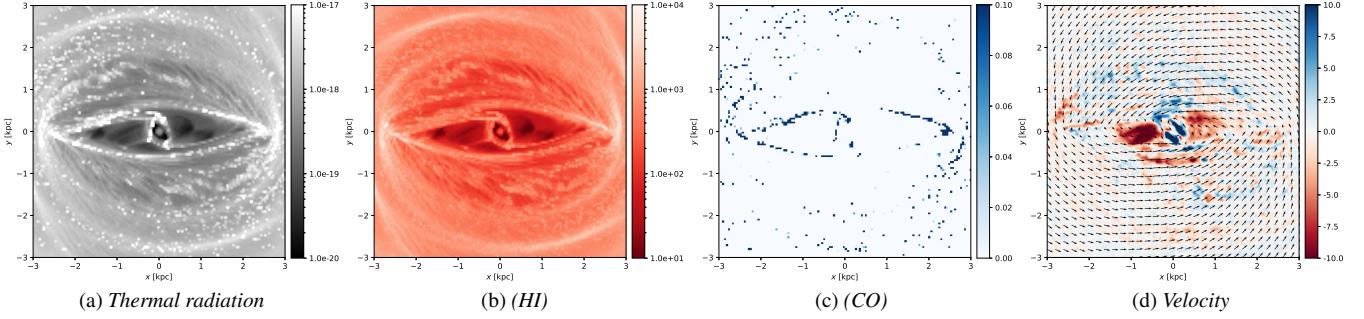


**Figure 11:** Top view of a subset of the attributes of the Galaxy dataset: (a) Density of CMZ dataset integrated along the line-of-sight, (b) density of hydrogen (HI), (c) density of carbon monoxide (CO), (d) color-coded line-of-sight velocity in [km/s], and tangential velocity shown using vector glyphs. Distances given in kiloparsec (kpc), where  $1 \text{ pc} \approx 3.26 \text{ ly} \approx 9.46 \times 10^{12} \text{ km}$ .

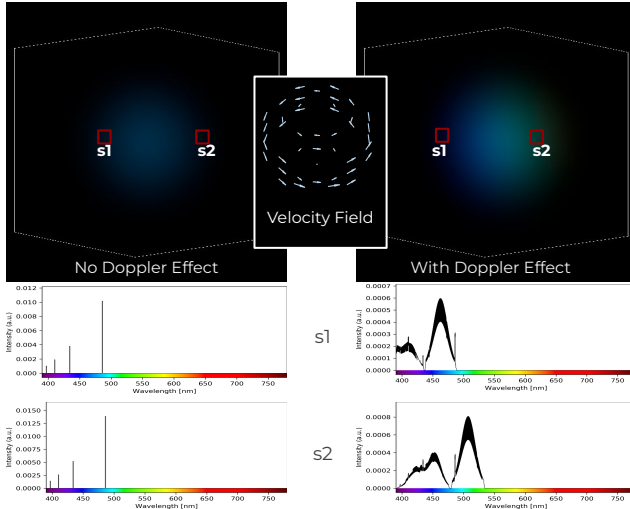


**Figure 12:** Synthetic Hydrogen dataset, with velocity field and two sample spectra:  $s_1$  exemplifying a blue-shift, and  $s_2$  a red-shift.

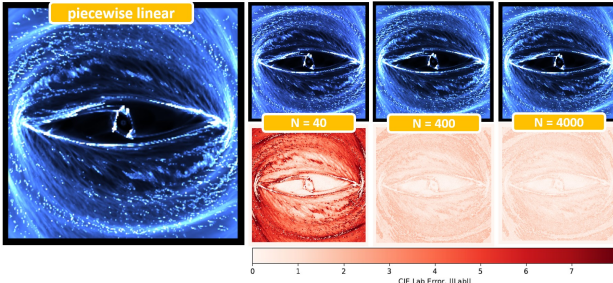


**Figure 13:** Comparison of Galaxy dataset black-body rendered either with piecewise linear functions (1433 ms) or with  $N$  bands using spectral point-sampling, with  $N = 40$  (340 ms),  $N = 400$  (1884 ms),  $N = 4000$  (2222 ms).

have a major impact when evaluating the Doppler effect. This is not only due to minor density in the dataset, but also because the curve generated by Planck's law can be approximated efficiently with a small number of segments in the piecewise linear functions

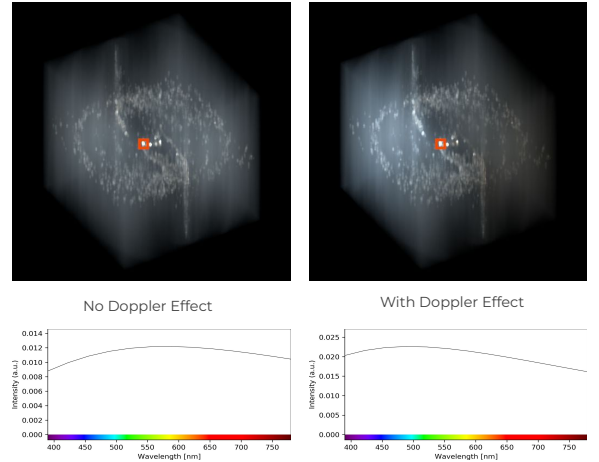


**Figure 14:** Piecewise linear spectral rendering of the black-body emission in the Galaxy dataset, without and with Doppler effect, and respective highlighted sample (red box) with corresponding spectrum (bottom). Note the blue shift in the shape of Planck's law for thermal radiation, similar to changing the temperature.

(Figure 10). On the other hand, light from line emission of the materials is more expensive to compute. As the number of delta peaks of the materials increases, each accumulation step adds more segments to the piecewise linear representation, multiplying the cases of addition between them. We can observe this at the combination of black-body emission, hydrogen, and a complex material like carbon (Figure 16), or in particular when adding the helium channel, which is not only the most complex, but also is widely distributed in the dataset (Figure 17). In such cases, even with the merging strategy from Section 4.2 enabled (Figure 18), the spectrum can become very complex (thousands of pieces), causing low rendering performance. In order to guarantee interactivity in such cases, we employ a simple preview strategy that reduces the number of samples of each ray while the user is actively moving the camera or changing parameters, if the complexity of the piecewise representation becomes too high. When interaction stops, the high-quality frame is rendered (see the video provided as supplemental material).

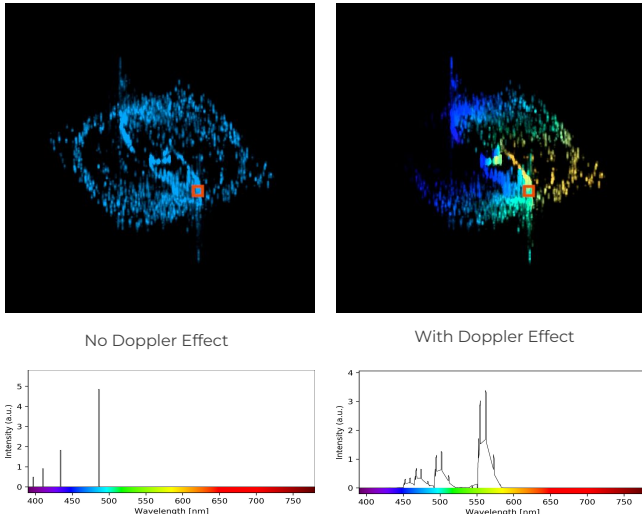


**Figure 15:** Piecewise linear spectral rendering of the Galaxy dataset, with emission from hydrogen only, and spectra (bottom) corresponding to respective samples (red boxes). Note the different colors emerging when the Doppler effect is taken into account, especially in the regions of the model with higher velocities.

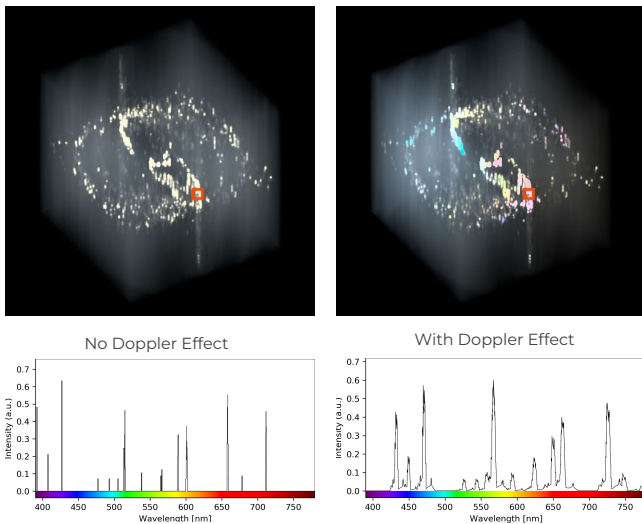


**Figure 16:** Piecewise linear spectral rendering of a view of the galaxy, with emission from hydrogen, carbon, and the black-body.

## 7. Conclusion

We investigated the use of the Doppler effect in spectral volume rendering for an emission-absorption model. We extended the typical volume rendering of scalar data to include a vector field, which causes the spectral deviations in absorption and emission according to the Doppler effect. To achieve this at interactive frame rates, we introduced a novel piecewise linear representation of spectra that enables more accurate and more efficient rendering through piecewise analytical accumulation and convolution. We tested our method with a galaxy formation simulation, and showed that it provides more accurate results and renders in less time than clas-

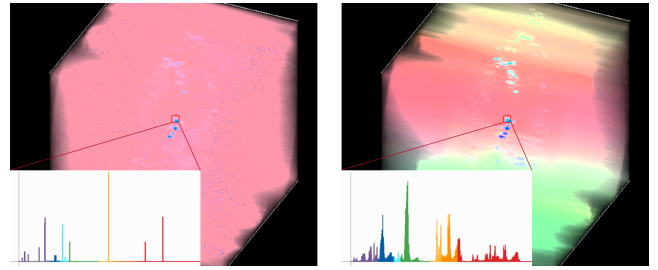


**Figure 17:** Piecewise linear spectral rendering of the Galaxy dataset, with emission from hydrogen, carbon, and helium. As helium fills the entire space and its emission lines are complex, the merge tolerance was relaxed for acceptable render times (Table 1).

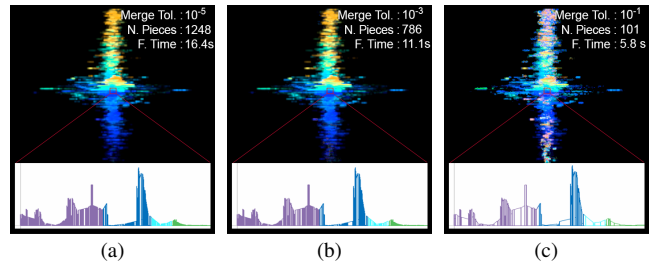


**Figure 18:** Effect of the merging optimization: as the tolerance is increased, the number of pieces representing the spectrum decreases and thus the rendering time, but at the cost of inaccuracies.

sic point-based spectral representation. While the method we presented provides accurate results, further work could be done to optimize the algorithm. In cases where the material exhibits many spectral delta peaks, the computational cost of accumulation can grow very fast. Similarly, when the ray accumulates many pieces of spectra, the cost of adding new ones increases quickly. These problems could be solved using more sophisticated data structures for managing the piecewise function, such as a binary tree, or by using a threshold that allows merging pieces of the function, at the cost of accuracy. Beyond this, we want to apply our technique to further cases, especially datasets with very high velocities and therefore strong Doppler effect. When considering such extreme velocities, one could also implement a relativistic Doppler effect, which should be an easy extension of our model. The presented model could also be extended to include other spectral effects. Since the optical information is available in spectral form, it is appealing to also investigate the incorporation of effects like diffraction.

## Acknowledgments

This work was supported in part by King Abdullah University of Science and Technology (KAUST), and by the Deutsche Forschungsgemeinschaft (DFG, German Research Foundation) under Germany's Excellence Strategy EXC2181/1-390900948 (the Heidelberg STRUCTURES Excellence Cluster). We thank Patrick Quicker for the development of the initial prototype as part of his BSc thesis, Ralf Klessen for fruitful discussions and the Galaxy dataset, and Marco Agus for his useful comments and suggestions.

## References

- [ARC05] ABDUL-RAHMAN A., CHEN M.: Spectral volume rendering based on the Kubelka-Munk theory. *Computer Graphics Forum* 24, 3 (2005), 413–422. [doi:10.1111/j.1467-8659.2005.00866.x](https://doi.org/10.1111/j.1467-8659.2005.00866.x). 3
- [ASDW14] AMENT M., SADLO F., DACHSBACHER C., WEISKOPF D.: Low-pass filtered volumetric shadows. *IEEE Transactions on Visualization and Computer Graphics* 20, 12 (2014), 2437–2446. [doi:10.1109/TVCG.2014.2346333](https://doi.org/10.1109/TVCG.2014.2346333). 3
- [ASW13] AMENT M., SADLO F., WEISKOPF D.: Ambient volume scattering. *IEEE Transactions on Visualization and Computer Graphics* 19, 12 (2013), 2936–2945. [doi:10.1109/TVCG.2013.129](https://doi.org/10.1109/TVCG.2013.129). 3
- [BMDF02] BERGNER S., MOLLER T., DREW M. S., FINLAYSON G. D.: Interactive spectral volume rendering. In *IEEE Visualization, 2002. VIS 2002.* (Oct 2002), pp. 101–108. [doi:10.1109/VISUAL.2002.1183763](https://doi.org/10.1109/VISUAL.2002.1183763). 2
- [BMTD05] BERGNER S., MOLLER T., TORY M., DREW M. S.: A practical approach to spectral volume rendering. *IEEE Transactions on Visualization and Computer Graphics* 11, 2 (March 2005), 207–216. [doi:10.1109/TVCG.2005.19](https://doi.org/10.1109/TVCG.2005.19). 2
- [BUT\*19] BOUSSEIRA M. O., UCHIKI R., TAKESHIMA Y., MATSUBAYASHI K., TAKEKAWA S., UEMURA M., FUJISHIRO I.: aftak: Visual programming environment enabling end-to-end provenance management for the analysis of astronomical datasets. *Visual Informatics* 3, 1 (2019), 1–8. Proceedings of PacificVAST 2019. [doi:https://doi.org/10.1016/j.visinf.2019.03.001](https://doi.org/10.1016/j.visinf.2019.03.001). 3
- [EKE01] ENGEL K., KRAUS M., ERTL T.: High-quality pre-integrated volume rendering using hardware-accelerated pixel shading. In *Proceedings of the ACM SIGGRAPH/EUROGRAPHICS Workshop on Graphics Hardware* (New York, NY, USA, 2001), HWWS ’01, Association for Computing Machinery, p. 9–16. URL: <https://doi.org/10.1145/383507.383515>, [doi:10.1145/383507.383515](https://doi.org/10.1145/383507.383515). 5
- [FDF94] FINLAYSON G. D., DREW M. S., FUNT B. V.: Spectral sharpening: sensor transformations for improved color constancy. *JOSA A* 11, 5 (1994), 1553–1563. 2
- [FK10] FOGAL T., KRÜGER J. H.: Tuvok, an architecture for large scale volume rendering. In *VMV* (2010), vol. 10, pp. 139–146. 7
- [HLSR09] HADWIGER M., LJUNG P., SALAMA C. R., ROPINSKI T.: GPU-Based Volume Ray-Casting with Advanced Illumination. In *Eurographics 2009 - Tutorials* (2009), Museth K., Weiskopf D., (Eds.), The Eurographics Association. [doi:10.2312/egt.20091069](https://doi.org/10.2312/egt.20091069). 2
- [K\*17] KARTTUNEN H., ET AL.: *Fundamental Astronomy*. Springer-Verlag, 2017. 3
- [KYRa17] KRAMIDA A., YU. RALCHENKO, READER J., AND NIST ASD TEAM: Nist atomic spectra database (ver. 5.10). <https://physics.nist.gov/asd>, 2017. 8
- [Lin] LINDBLOM B.: online: [http://www.brucelindblom.com/index.html?Eqn\\_RGB\\_XYZ\\_Matrix.html](http://www.brucelindblom.com/index.html?Eqn_RGB_XYZ_Matrix.html). 4
- [MTW73] MISNER C., THORNE K., WHEELER J.: *Gravitation*. W. H. Freeman, 1973. 4
- [NvdVS00] NOORDMANS H. J., VAN DER VOORT H. T. M., SMEULDERS A. W. M.: Spectral volume rendering. *IEEE Transactions on Visualization and Computer Graphics* 6, 3 (July 2000), 196–207. [doi:10.1109/2945.879782](https://doi.org/10.1109/2945.879782). 2
- [Pee93] PEERCY M. S.: Linear color representations for full speed spectral rendering. In *Proceedings of the 20th Annual Conference on Computer Graphics and Interactive Techniques* (New York, NY, USA, 1993), SIGGRAPH ’93, ACM, pp. 191–198. [doi:10.1145/166117.166142](https://doi.org/10.1145/166117.166142). 2
- [RF91] RASO M. G., FOURNIER A.: A piecewise polynomial approach to shading using spectral distributions. In *Proceedings of Graphics Interface ’91* (1991), GI ’91, pp. 40–46. [doi:10.20380/GI1991.06](https://doi.org/10.20380/GI1991.06). 2
- [RGG\*13] RODRIGUEZ M. B., GOBBETTI E., GUITIÁN J. A. I., MAKHINYA M., MARTON F., PAJAROLA R., SUTER S. K.: A survey of compressed gpu-based direct volume rendering. In *Eurographics (State of the Art Reports)* (2013), pp. 117–136. 7
- [Rin04] RINDLER W.: *Relativity - Special, General and Cosmology*. Oxford University Press, 2004. 4
- [SFDC01] SUN Y., FRACCHIA F. D., DREW M. S., CALVERT T. W.: A spectrally based framework for realistic image synthesis. *The Visual Computer* 17 (October 2001), 429–444. 2
- [SKB\*06] STRENGERT M., KLEIN T., BOTCHEN R., STEGMAIER S., CHEN M., ERTL T.: Spectral volume rendering using gpu-based ray-casting. *The Visual Computer* 22, 8 (2006), 550–561. [doi:10.1007/s00371-006-0028-0](https://doi.org/10.1007/s00371-006-0028-0). 3
- [SKW\*10] STEFFEN W., KONING N., WENGER S., MORISSET C., MAGNOR M.: Shape: A 3d modeling tool for astrophysics. *IEEE Transactions on Visualization and Computer Graphics* 17, 4 (2010), 454–465. 3
- [Spr10] SPRINGEL V.: E pur si muove: Galilean-invariant cosmological hydrodynamical simulations on a moving mesh. *Monthly Notices of the Royal Astronomical Society* 401, 2 (2010), 791–851. [doi:10.1111/j.1365-2966.2009.15715.x](https://doi.org/10.1111/j.1365-2966.2009.15715.x). 8
- [STR\*18] SORMANI M. C., TRESS R. G., RIDLEY M., GLOVER S. C. O., KLESSEN R. S., BINNEY J., MAGORRIAN J., SMITH R.: A theoretical explanation for the central molecular zone asymmetry. *Monthly Notices of the Royal Astronomical Society* 475, 2 (2018), 2383–2402. [doi:10.1093/mnras/stx3258](https://doi.org/10.1093/mnras/stx3258). 7
- [UBZ\*20] UCHIKI R., BOUSSEJRA M. O., ZHU L., TAKESHIMA Y., MATSUBAYASHI K., UEMURA M., FUJISHIRO I.: Accurate Visualization of Galaxy Velocity Fields from Three-Dimensional Integral Field Spectroscopy Data. In *EuroVis 2020 - Posters* (2020), Byška J., Jánicek S., (Eds.), The Eurographics Association. [doi:10.2312/eurp.20201123](https://doi.org/10.2312/eurp.20201123). 3
- [WKR99] WEISKOPF D., KRAUS U., RUDER H.: Searchlight and doppler effects in the visualization of special relativity: A corrected derivation of the transformation of radiance. *ACM Trans. Graph.* 18, 3 (jul 1999), 278–292. URL: <https://doi.org/10.1145/336414.336459>, [doi:10.1145/336414.336459](https://doi.org/10.1145/336414.336459). 3
- [WS00] WYSZECKI G., STILES W. S.: *Color science: concepts and methods, quantitative data and formulae*. John Wiley & Sons, 2000. 4

# Doppler Volume Rendering: A Dynamic, Piecewise Linear Spectral Representation for Visualizing Astrophysics Simulations.

## Supplemental Material

Reem Alghamdi<sup>1</sup>, Thomas Müller<sup>2</sup>, Alberto Jaspe-Villanueva<sup>1</sup>, Markus Hadwiger<sup>1</sup>, Filip Sadlo<sup>3</sup>

<sup>1</sup>KAUST, Saudi Arabia, <sup>2</sup>Max-Planck-Institute for Astronomy, Germany, <sup>3</sup>Heidelberg University, Germany

### 1. Accumulation Cases

The mathematical formulation for all the possible 11 accumulation cases of  $f(x)$  and  $g(x)$  piecewise linear functions is as follows:

Case	Accumulation	Case	Accumulation
Case 1 or 11: $x_2 < y_1 \vee y_2 < x_1$	$f(x) + g(x) =$ $\begin{cases} m_1x + b_1 & x_1 \leq x \leq x_2 \\ m_2x + b_2 & y_1 \leq x \leq y_2 \\ 0, & \text{else} \end{cases}$	Case 2: $x_1 < y_1 < x_2 < y_2$	$f(x) + g(x) =$ $\begin{cases} m_1x + b_1 & x_1 \leq x \leq y_1 \\ (m_1 + m_2)x + (b_1 + b_2) & y_1 < x \leq x_2 \\ m_2x + b_2 & x_2 < x \leq y_2 \\ 0, & \text{else} \end{cases}$
Case 3: $y_1 < x_1 < y_2 < x_2$	$f(x) + g(x) =$ $\begin{cases} m_2x + b_2 & y_1 \leq x \leq x_1 \\ (m_1 + m_2)x + (b_1 + b_2) & x_1 < x \leq y_2 \\ m_1x + b_1 & y_2 < x \leq x_2 \\ 0, & \text{else} \end{cases}$	Case 4: $x_1 < y_1 < x_2 = y_2$	$f(x) + g(x) =$ $\begin{cases} m_1x + b_1 & x_1 \leq x \leq y_1 \\ (m_1 + m_2)x + (b_1 + b_2) & y_1 < x \leq y_2 \\ 0, & \text{else} \end{cases}$
Case 5: $x_1 = y_1 < x_2 = y_2$	$f(x) + g(x) =$ $\begin{cases} (m_1 + m_2)x + (b_1 + b_2), & x_1 \leq x \leq x_2 \\ 0, & \text{else} \end{cases}$	Case 6: $y_1 < x_1 < x_2 = y_2$	$f(x) + g(x) =$ $\begin{cases} m_2x + b_2 & y_1 \leq x \leq x_1 \\ (m_1 + m_2)x + (b_1 + b_2) & x_1 < x \leq y_2 \\ 0, & \text{else} \end{cases}$
Case 7: $x_1 = y_1 < x_2 < y_2$	$f(x) + g(x) =$ $\begin{cases} (m_1 + m_2)x + (b_1 + b_2) & x_1 \leq x \leq x_2 \\ m_2x + b_2 & x_2 < x \leq y_2 \\ 0, & \text{else} \end{cases}$	Case 8: $x_1 = y_1 < x_2 < y_2$	$f(x) + g(x) =$ $\begin{cases} (m_1 + m_2)x + (b_1 + b_2) & x_1 \leq x \leq y_2 \\ m_1x + b_1 & y_2 < x \leq x_2 \\ 0, & \text{else} \end{cases}$
Case 9: $x_1 < y_1 < y_2 < x_2$	$f(x) + g(x) =$ $\begin{cases} m_1x + b_1 & x_1 \leq x \leq y_1 \\ (m_1 + m_2)x + (b_1 + b_2) & y_1 < x \leq y_2 \\ m_1x + b_1 & y_2 < x \leq x_2 \\ 0, & \text{else} \end{cases}$	Case 10: $y_1 < x_1 < x_2 < y_2$	$f(x) + g(x) =$ $\begin{cases} m_2x + b_2 & y_1 \leq x \leq x_1 \\ (m_1 + m_2)x + (b_1 + b_2) & x_1 < x \leq x_2 \\ m_2x + b_2 & x_2 < x \leq y_2 \\ 0, & \text{else} \end{cases}$

## 2. Galaxy Dataset Information

Additional information of the Galaxy dataset, simulating the asymmetries of the center of the Milky Way, by Sormani et al.:

Density range	$\rho \in [7.65 \times 10^{-26} \text{ g/cm}^3, 1.94 \times 10^{-15} \text{ g/cm}^3]$ $\rho_{q=0.05} = 8.1 \times 10^{-23} \text{ g/cm}^3$ , $\rho_{q=0.95} = 3.16 \times 10^{-20} \text{ g/cm}^3$
Gas temperature range	$T \in [130.7 \text{ K}, 481.1 \text{ K}]$ $T_{q=0.05} = 439.0 \text{ K}$ , $T_{q=0.95} = 480.9 \text{ K}$
Velocity ranges	$v_x \in [-342, 328] \text{ km/s}$ , $v_y \in [-238, 242] \text{ km/s}$ , $v_z \in [-140, 117] \text{ km/s}$ $v_{x,q=0.05} = -267 \text{ km/s}$ , $v_{x,q=0.95} = 267 \text{ km/s}$ $v_{y,q=0.05} = -200.0 \text{ km/s}$ , $v_{y,q=0.95} = 200 \text{ km/s}$ $v_{z,q=0.05} = -10.0 \text{ km/s}$ , $v_{z,q=0.95} = 9.39 \text{ km/s}$ (Compare Speed-of-light $c = 299\,792.458 \text{ km/s}$ )
Matter included	neutral hydrogen $HI$ molecular hydrogen $H_2$ carbon monoxide $CO$

## 3. Synthetic Dataset

With the aim of evaluating our technique in a controlled environment, we created a synthetic dataset, consisting of a radial density field of hydrogen, moved by a vector field with cylindrical dynamics, of thickness around 10% of the side of the volume. The figure shows two sample spectra along respective rays traversing the velocity field.

